Radiative Transfer Modeling of Chang'e-4 Spectroscopic Observations and Interpretation of the South Pole-Aitken Compositional Anomaly

Jian Chen[1], Zongcheng Ling[1], Bradley L. Jolliff[2], Lingzhi Sun[3], Le Qiao[1] , Jianzhong Liu[4], Xiaohui Fu[1], Jiang Zhang[1] , Bo Li[1], Changqing Liu[1], Xiaobin Qi[1], Xuejin Lu[1], Zhiping He[5], and Rui Xu[5]

[1] Shandong Key Laboratory of Optical Astronomy and Solar-Terrestrial Environment, Institute of Space Sciences, Shandong University, Weihai, 264209, People's Republic of China; zcling@sdu.edu.cn
[2] Department of Earth & Planetary Sciences and the McDonnell Center for the Space Sciences, Washington University, St. Louis, MO 63130, USA
[3] Hawai'i Institute of Geophysics and Planetology, Department of Earth Sciences, University of Hawai'i at Mānoa, Honolulu, HI 96826, USA
[4] Institute of Geochemistry, Chinese Academy of Sciences, Guiyang, 550002, People's Republic of China
[5] Key Laboratory of Space Active Opto-Electronics Technology, Shanghai Institute of Technical Physics, Chinese Academy of Sciences, Shanghai, 200083, People's Republic of China

Abstract

Chang'e-4 landed in the Von Kármán basaltic zone affected by Finsen ejecta from the South Pole-Aitken (SPA) "compositional anomaly" (SPACA), providing an opportunity to untangle the origin of the SPACA. We developed a mineral abundance unmixing model and built a spectral library composed of mineral mixtures of plagioclase, low-Ca pyroxene, high-Ca pyroxene, and olivine. Based on the mineral abundances returned by our model, the average plagioclase abundance (60.4 vol.%) of SPACA is beyond the high-plagioclase end of the mineralogical range of SPA impact melt differentiation products and would require an additional contribution from crustal materials. We suggest that either the crust was not entirely removed in the SPA-forming impact or the ejecta from post-SPA basins fed feldspathic materials back onto the SPA basin floor. Our unmixing analyses indicate that the surface regolith of the SPACA is a mixture of 70.2% crustal materials and 29.8% Fe- and incompatible-element-enriched materials.

1. Introduction

The South Pole-Aitken (SPA) basin, located on the Moon's farside southern hemisphere, is the largest confirmed impact structure and one of the most diversified geochemical provinces on the Moon (Spudis et al. 1994). The SPA basin holds keys to unlock the secrets of lunar evolution with its unique characteristics: a spatial location around the antipode of the nearside Procellarum KREEP terrane, as a potential cause of lunar global asymmetry, its vast size as a boundary condition for modeling and simulation of lunar impact processes, its antiquity as an ideal anchor for the early history of the Moon, and unusual materials as possible outcrops of lunar deep strata (Jolliff et al. 2006). These characteristics make the SPA basin an excellent target for investigating the evolution of the Moon. Among its various characteristics, the nonmare mafic anomaly associated with the interior of the SPA basin has attracted wide attention from the lunar scientific community since it was fully mapped by the Clementine mission (Spudis et al. 1994).

The formation of the SPA basin is thought to have penetrated into the lunar interior and exposed deep (lower crust and/or upper mantle) materials (Potter et al. 2012). This interpretation is supported by elevated concentrations of mafic components and incompatible elements such as thorium inside the basin compared with adjacent feldspathic highlands (Figure A1). Various orbital spectroscopic data sets indicate that the mafic mineralogy of the SPA basin floor is dominated by pyroxene (e.g., Pieters et al. 1997), and few olivine-rich exposures were observed within the SPA basin (e.g., Yamamoto et al. 2010). Heterogeneous pyroxene compositions were subsequently observed within the SPA basin using hyperspectral remote-sensing data sets (Moriarty 2016). Based on the pyroxene compositions, the interior of the SPA basin was further divided into several subunits, one of which exhibits unusual pyroxene compositions and was defined as the SPA compositional anomaly (SPACA). Different scenarios were proposed to explain the characteristics of the SPACA region; however, the origin of the unusual mineralogy remains uncertain with limited knowledge of the actual pyroxene composition.

In addition to the possible direct exposure of materials from the deep interior, the unusual materials within the basin have also been considered as products of the SPA impact melt sheet. The energetic SPA impact event is expected to have produced a large volume of melt (Melosh et al. 2017). The pervasive noritic lithology in the SPA basin floor has been suggested to be either an undifferentiated impact melt sheet, reflecting the bulk composition of the lower crust (e.g., Pieters et al. 1997) or the top layer of a differentiated melt beginning from an ultramafic composition representing the upper mantle (Nakamura et al. 2009). Numerous contributions have documented observations and simulations to constrain models of SPA impact and melting processes; however, the composition of the melt and source materials is still under debate with regard to the SPACA.

The Chang'e-4 (CE-4) landing region was initially selected using technical constraints, i.e., a safe location (Jia et al. 2018)
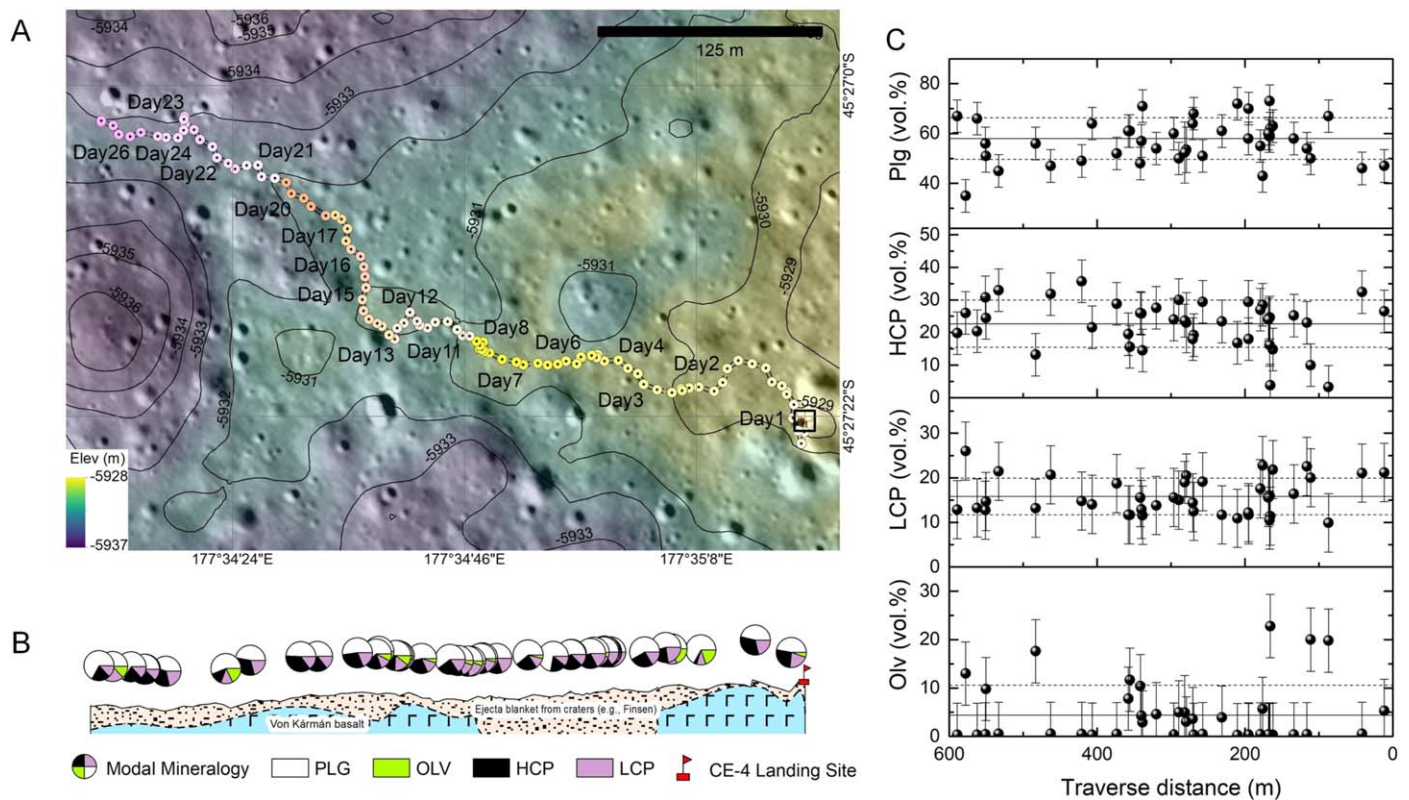
Figure 1. Yutu-2 traverse map and mineralogical variations along the path. (A) Traverse path of the Yutu-2 rover and locations of the exploration sites overlaid on the image taken by LROC NAC (frame M1303619844) and the color-coded digital terrain mode (DTM) derived from stereo pairs of NAC images (https://wms.lroc.asu. edu/lroc/view_rdr/NAC_DTM_CHANGE4). Topographic contours are shown as black solid lines with the elevation values labeled. (B) Shallow subsurface stratigraphy along the traverse path. The thicknesses of different deposit layers reflect the mixing ratios. The vertical scale is zoomed 10×. (C) Estimated mineralogy along the traverse path. The solid and dashed lines indicate the mean values and standard deviations of mineral proportions.

(The data used to create this figure are available.)

on the lunar farside. Hence, the smooth mare plains in the Von Kármán crater were chosen with the scientific objective to explore the farside volcanism that occurred in the SPA basin, whereas subsequent geological and spectroscopic characterizations of the CE-4 mission target region from orbit revealed that the basaltic deposits in the Von Kármán crater floor have been mostly obscured by nonmare crater ejecta (Qiao et al. 2019). Given that the unusual pyroxene compositions of the SPACA were also observed on the wall of the Finsen crater (Moriarty 2016), the spectral measurements of materials ejected from the Finsen crater wall (FW) by the CE-4 visible and near-infrared imaging spectrometer (VNIS) with an unprecedented spatial resolution are expected to help explore in detail the mineralogy in the SPACA.

Since the successful landing of CE-4 and the deployment of the Yutu-2 rover in 2019 January (Di et al. 2019), a number of morphological and mineralogical results have been reported (Gou et al. 2019; Hu et al. 2019; Li et al. 2019; Huang et al. 2020; Chen et al. 2020; Lin et al. 2020; Ma et al. 2020). There is consensus that the surface regolith at the CE-4 exploration region is affected by Finsen crater ejecta; however, the mineralogy and petrogenetic origin of these materials remains controversial.

To constrain the regolith mineralogy at the CE-4 landing region and understand the processes that generated the unusual materials in the SPACA, we carried out comprehensive mineralogical analyses utilizing data collected by the VNIS

in the first 26 lunar days of the CE-4 mission (Figure 1). The modal mineralogy and compositions of major silicate minerals (i.e., plagioclase (Plg), low-Ca pyroxene (LCP), high-Ca pyroxene (HCP), and olivine (Olv)) in the regolith were determined using a spectral look-up table (LUT) constructed using the Hapke radiative transfer model (RTM). Unmixing analysis was further conducted based on the mineralogical and compositional results, aiming to evaluate the contributions of different potential reservoirs to the observed mineralogy in the regolith at the CE-4 landing region as well as in the SPACA.

2. Data and Methods

The Yutu-2 rover traversed ∼628 m in the first 26 lunar days (Figure 1). The VNIS aboard the Yutu-2 rover collected 120 hyperspectral visible and near-infrared (VNIR) images (450–950 nm) and single-pixel short-wave infrared (SWIR) spectra (900–2400 nm) for 54 soil-dominated targets and four boulders. The complete figure set (120 images of Yutu-2 VNIS targets) is available. The VNIS raw data were processed to level 2B radiance through a series of processing pipelines including dark-current, scattering-background subtractions, flat-field, instrument temperature corrections, and radiometric and geometric calibrations (Liu et al. 2014). The data were then distributed by the Ground Research and Application System (GRAS) of the Chinese Lunar Exploration Program. For the convenience of readers, VNIS images and spectra are labeled by the sequence numbers as shown in the filenames released by

GRAS (e.g., 0001 for CE4_GRAS_VNIS*N_yyyymmddhh-miss_YYYYMMDDMISS_0001*.2B data) rather than the engineering labels used by other publications. The level 2B VNIS radiance data were further processed (e.g., solar distance correction) to derive a credible reflectance factor (REFF) for quantitative mineralogical analyses. A detailed description of processing procedures can be found in the appendices and our previous publication (Chen et al. 2020).

2.1. Correction of Instrumental Artifacts

An artifact absorption around 820 nm (Figure A2) is noticed in VNIS spectra and is probably caused by the F46 films in the multilayer insulation (Xu et al. 2021) on the body and/or aluminum metal in the wheels of the Yutu-2 rover. This artifact is more obvious in VNIS spectra of darker pixels where the sunlight is shielded by local topography while the reflected and/or scattered sunlight with 820 nm absorption from the rover serves as a dominant light source. Besides introducing an additional absorption, the artifact is expected to affect the short-wavelength shoulder position of 1 μm absorption in VNIS spectra (Figure A2). Furthermore, spectra with such an artifact used for matching with the spectral library would tend to generate a modal mineralogy with more olivine because olivine has a broader absorption than pyroxene (Figure A2). Thus, in order to identify and remove this artifact, the integrated band depth (IBD) of the 820 nm feature (IBD820) was calculated by fitting a linear continuum over the feature and then integrating the band depths relative to the continuum at each wavelength within the regions (Table A1). The pixels with IBD820 greater than 0.01 were referred to as affected by this artifact.

In addition, significant darkening effects on the reflectance owing to shadows in the VNIR image caused by surface roughness were observed and relevant correction is also necessary. The pixels with REFF at 465 nm less than 0.02 were regarded as shadows. Both bright pixels with 820 nm artifacts and dark/shadow pixels are removed when calculating the average VNIR reflectance in the FOV (field of view) of SWIR detectors.

2.2. Photometric Correction

As the CE-4 VNIS measurements were performed at large phase angles (~40°–117°), photometric correction is important for comparisons of reflectance spectra taken under different illumination conditions and further quantitative analysis of mineral abundances for local regolith. The standard deviations of mineral abundances of the same target derived from raw spectra (without photometric correction) and photometrically corrected spectra would be as large as 12.3 vol.%, 9.2 vol.%, 4.8 vol.%, and 7.6 vol.% for Plg, HCP, LCP, and Olv, respectively. Photometric models for local regolith at the CE-4 landing region have been obtained from VNIS data collected on the 10th lunar day when spectral measurements of the same target at various illumination geometry were done by the Yutu-2 rover. The VNIS spectra of local soils at the CE-4 landing region were corrected to REFF at standard illumination geometry ($i = 30°$, $e = 0°$, and $g = 30°$) using the Lommel–Seeliger (LS) model (Qi et al. 2020). Although the LS model is a highly simplified solution of the Hapke RTM with the assumption of isotropic single scattering without multiple scattering, this empirical model somehow works better for photometric correction of CE-4 VNIS data sets than Hapke's

RTM. After the photometric correction, the spectral discrepancy of the same target collected at different viewing geometries was suppressed to ~3.7% with the LS model and ~7.4% with the Hapke model (Qi et al. 2020). The residual errors of mineralogy (standard deviations of the same target) derived from LS-model photometrically corrected spectra are 1.1 vol.%, 0.6 vol.%, 0.5 vol.%, and 2.0 vol.% for Plg, HCP, LCP, and Olv, respectively.

2.3. Modal Mineralogy and Mafic Mineral Compositions

The LUT of modeled REFF spectra using Hapke's RTM was constructed to compare with the observed REFF spectra by CE-4 VNIS. Abundances of mineral end-members composing the CE-4 regolith were derived via minimizing the rms errors (RMSE) and spectral angle (SA) between observed VNIS spectra and modeled spectral LUT. The detailed description of Hapke's RTM used in this work can be found in Appendix A.1. The modeled spectral LUT contains REFF spectra of 323,449,000 mixtures of Olv ($Fo_{75} \sim Fo_{64}$), LCP ($Fs_{27}Wo_1En_{72} \sim Fs_{31}Wo_{20}En_{49}$), HCP ($Fs_{16}Wo_{40}En_{44} \sim Fs_{31}Wo_{20}En_{49}$), and Plg ($An_{95}Ab_5$). The uncertainties of this model in estimating mineral abundance are better than 4 vol.% for LCP and HCP, better than 5 vol.% for Olv, and better than 6 vol.% for Plg. In this work, the model is validated using 19 Apollo soil samples (Figure 2).

The agglutinitic glass is the dominant (30–70 vol.%; Taylor et al. 2001) component in lunar soils, while the absorption characteristics in VNIS spectra of soils at the CE-4 landing region resemble crystalline phases. Mafic glass and mafic minerals exhibit similar 1 μm absorption bands, the position and strength of which depend on the composition and cooling rate. If impact melts cooled slowly enough for recrystallization to occur, their spectra would resemble those of mafic minerals with similar compositions (Tompkins & Pieters 2010). Hence, it is expected that a proportion of the mafic mineral abundances reported in CE-4 regolith is probably recrystallized from impact melts. Given the overlapping 1 μm absorption features of agglutinitic glass and olivine, the incorporation or exclusion of glass may have an impact on the LUT model-retrieved results of olivine abundance. Compared to the spectral LUT without glass, the spectral LUT with glass improved the abundance retrieval accuracy of olivine (4.2 vol.% → 1.9 vol.%) for LSCC (Lunar Soil Characterization Consortium) samples while reducing the accuracies of LCP (3.8 vol.% → 4.7 vol.%), HCP (3.4 vol.% → 4.1 vol.%), and Plg (5.4 vol.%→8.0 vol.%) abundances as well as the total performance of the model (RMSE 6.5 vol.% → 8.4 vol.%). Thus, our spectral LUT only includes abundances of Plg, LCP, HCP, and Olv. The space-weathering effects were modeled with npFe and SMFe abundances.

3. Observations

3.1. Spectral Properties

The CE-4 VNIS spectra of soils are similar to the spectra of the CE-4 landing region, remotely observed by orbital spectrometers (Figure 3). Both orbital and ground spectra of the CE-4 exploration region are composed of reddish continuum and weak 1 μm and 2 μm absorption bands, suggesting that the soils are heavily space-weathered products from mafic-mineral-bearing lithologies. Among the detection targets, the spectra of boulders exhibit relatively higher
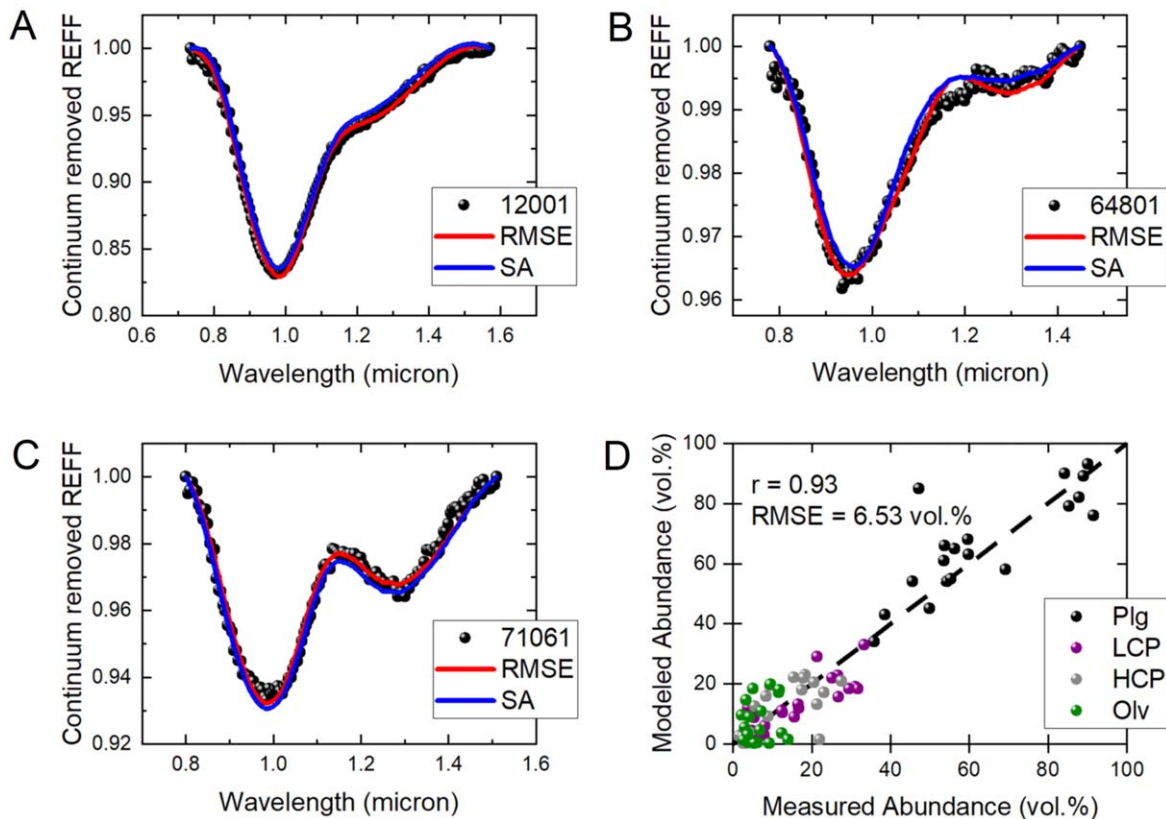
Figure 2. Comparison between the modeled and measured data. (A)–(C) LSCC spectra of samples 12001, 64804, and 71061 and their best-matched modeled spectra. (D) Mineral abundances modeled with our LUT vs. measured modal mineralogy of LSCC samples.

(The data used to create this figure are available.)

reflectance and stronger 1 μm and 2 μm absorption band strengths, which are consistent with their immature nature.

Multiple measurements on different parts of boulders (Figure A3) that demonstrated spectral variations with maturity were conducted. The more mature parts of the three boulders exhibit lower reflectance and weaker mafic absorption bands than their immature parts (Figure 3). These trends are consistent with the common observations of lunar space weathering: As the boulder is weathered to form regolith, it becomes darker and the mafic absorption strength decreases (Pieters et al. 2000). However, a difference is noted wherein the spectral slope of boulders decreases with increasing maturity. In other words, the more mature regolith tends to be bluer than less mature boulders, contrasting with the reddening effects of nanophase metallic Fe (npFe, tens of nanometers) residing in rims of mineral grains in lunar-style space weathering (e.g., Pieters et al. 2000). An alternative explanation to the observation of bluer spectra for more mature soils is the effects of larger-sized (>50 nm) submicroscopic metallic Fe (SMFe) in the interior of agglutinates that mainly darken but do not redden the host materials (Lucey & Riner 2011). Combined with reddish spectra of boulders, a two-stage space-weathering model could be inferred: (1) During space weathering of freshly exposed rocks, the decrease in the filling factor (increase of the porosity) decreased the reflectance (Hapke 2008) and the npFe formation further darkened the rock and reddened the spectral slope. (2) As the metallic Fe aggregates, larger-sized SMFe particles began to dominate the space-weathering effects that generated dark and flat spectra for

highly mature soils. The average abundances of npFe and SMFe in CE-4 soils were estimated to be, respectively, 0.22 wt. % and 0.23 wt.%, which are comparable to some Apollo and Luna soils (e.g., 15601; Morris 1980). The less mature parts of the boulders exhibit higher npFe abundances (0.14 wt.%) and lower SMFe abundances than their more mature parts (0.11 wt. % npFe and 0.03 wt.% SMFe), which is consistent with the redder and brighter spectra.

3.2. Modal Mineralogy

The CE-4 VNIS spectra and LUT-derived modal mineralogy of soils exhibit extensive mixing between the continuous ejecta of Finsen (hypothesized SPACA component excavated from FW) and local Von Kármán basalts (VKB, Figures 1, A4, A5, and A6), which was interpreted by Huang et al. (2020) as lithologic diversity. The average modal mineralogy of soils in the CE-4 landing region is 57.0 vol.% Plg, 15.8 vol.% LCP, 22.7 vol.% HCP, and 4.4 vol.% Olv, which are consistent with some previous researchers working on CE-4 VNIS data (56%–72% Plg, 9%–28% LCP, 4%–19% HCP, and 2%–12% Olv, Hu et al. 2019) within the model uncertainties.

3.3. Mafic Phases

The mafic mineralogy in the CE-4 regolith returned from LUT spectral matching further supports our preliminary conclusion based on spectral and mineralogical indices (Chen et al. 2020). The mafic assemblages in soils are dominated by pyroxenes (38.5 vol.%, 8–10 times the olivine proportion
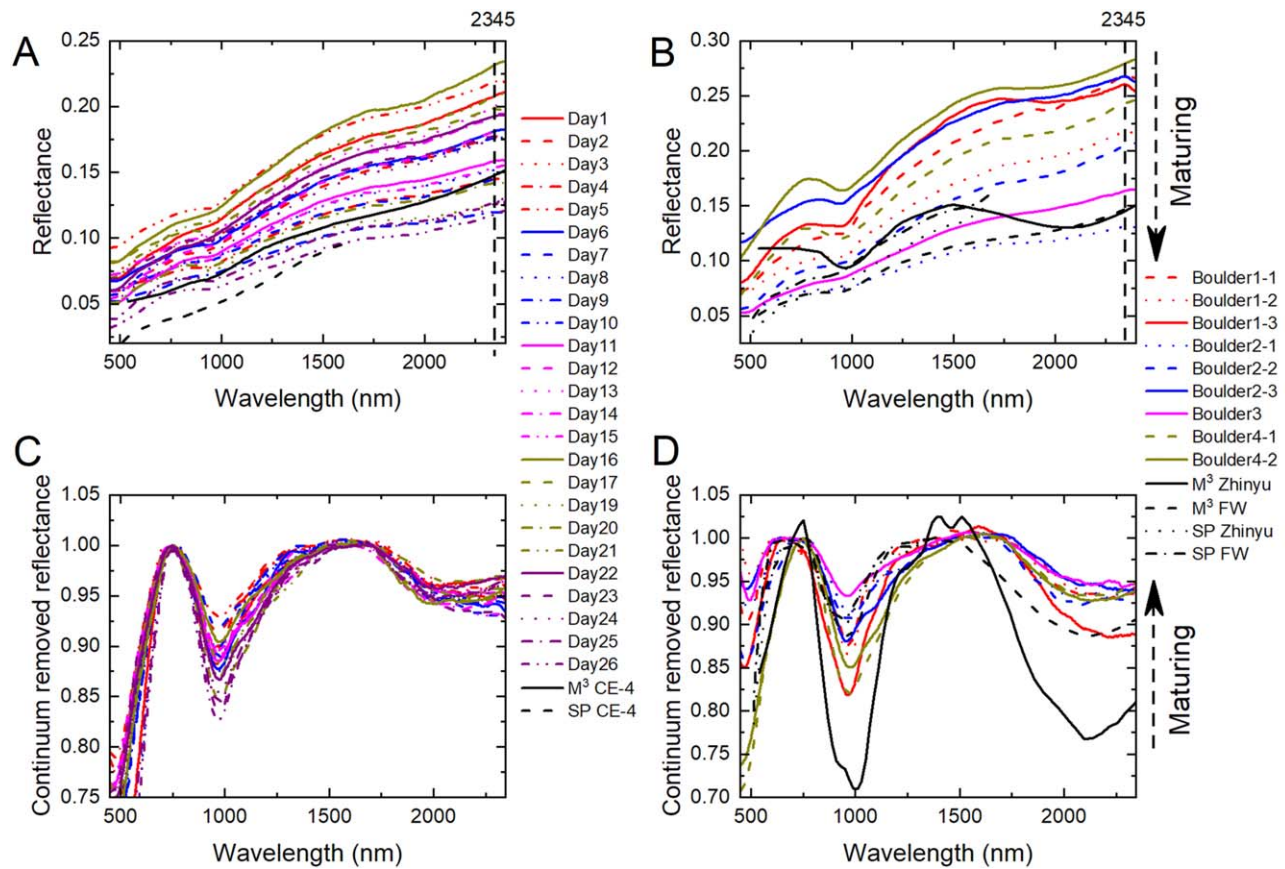
Figure 3. Comparison of orbital and ground spectra. (A)–(B) Average CE-4 VNIS spectra of soils and boulders compared with M^3 and SP spectra of the CE-4 landing region, Zhinyu crater, and FW. The reflectance is the REFF calibrated to the RELAB standard illumination geometry ($i = 30°$, $e = 0°$, and $g = 30°$). (C)–(D) Continuum-removed spectra. The arrows indicate the trend of maturation by space weathering. The average spectrum of the multiple measurements in each lunar day is compared here. The complete spectral figure set (54 images) is available online.

(The data used to create this figure are available.)

(The complete figure set (54 images) is available.)

(4.4 vol.%)). The relative proportions of LCP and HCP in soils are comparable to each other. It is also supported by the intermediate band centers (970.0 ± 5.2 nm) between LCP and HCP. Pyroxenes in soil targets exhibit extensive compositional distribution, and the most abundant pyroxene compositions are $Fs_{18.2}Wo_{48.0}En_{33.8}$ and $Fs_{34.7}Wo_{1.0}En_{64.4}$ for LCP and HCP, respectively.

The olivine-rich mineralogy as reported in previous studies on soil spectra (e.g., Li et al. 2019) is likely to be an artifact caused by the inappropriate continuum removal method and the 820 nm artifact. The convex-hull method was used by Li et al. (2019) to estimate the continuum of VNIS spectra where the last bands (2345–2395 nm) are on the hull, while these bands should not be on the continuum because the 2 μm absorption was not completely measured by VNIS (Figure A2). Such a continuum, connecting the short-wavelength edge of 2 μm absorption and the endpoint of VNIS spectra, significantly attenuates the true absorption strength at 2 μm and generates the illusion that the 2 μm absorption of VNIS spectra is weak and the soil of the CE-4 landing site is rich in olivine. In other words, the convex-hull method is not suitable for continuum removal with respect to the 2 μm absorption of VNIS spectra. Although the convex-hull method works well to remove the continuum of the 1 μm absorption, the resulting long-wavelength edges of 1 μm absorption in CE-4 VNIS spectra

are located at ∼1400–1500 nm, which is different from that of olivine-dominated spectra (typically at ∼1700 nm).

4. Discussion

The compositional and mineralogical remote sensing of SPACA indicates that plagioclase (58.4–60.4 vol.%) is more abundant than mafic minerals (39.6–41.6 vol.%, Lemelin et al. 2016) and imparts a crustal signature to the SPACA regolith. The plagioclase-rich mineralogy was interpreted to be from the plagioclase-rich crust formed by the differentiated SPA impact melt sheet (Hu et al. 2019). However, the SPACA is located within the assumed transient cavity formed by the SPA impact event (Figure A1) where all of the ∼45 km thick and feldspathic crust was thought to have been completely removed (Potter et al. 2012) and deposited far (>200 km distance) beyond the SPACA. Beginning from a mafic-rich bulk composition (23.3–49.1 wt.% FeO+MgO, 0.9–13.2 wt.% Al_2O_3), the differentiation of the SPA impact melt sheet is not expected to fractionate plagioclase from the residual melt and produce a secondary plagioclase-rich (Plg >60 vol.%) crust (Hurwitz & Kring 2014). Instead, the final mineral assemblage after fractional crystallization is likely plagioclase + ferran (Mg# = 5.1–68.7) mafic minerals that form noritic (HCP/LCP = 0.16–0.24) lithologies with relatively low Al compositions (10.9–14.5 wt.%). The average plagioclase
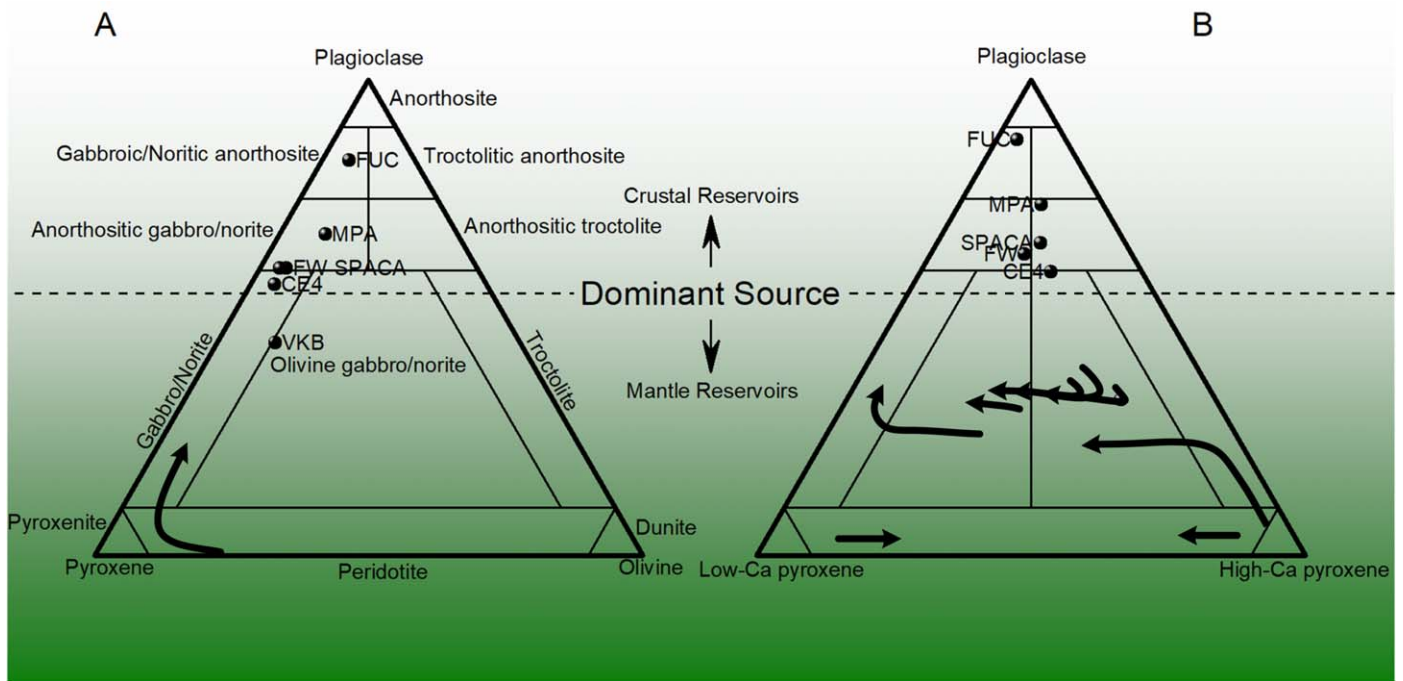
Figure 4. Mineralogy of CE-4 VNIS exploration sites. (A) Modal mineralogy plotted on a plagioclase–pyroxene–olivine ternary. (B) Modal mineralogy plotted on a Plg–LCP–HCP ternary (Olv < 10 vol.%). The modeled SPA impact melt differentiation and mineralogic evolution are indicated by arrows (Hurwitz & Kring 2014).
(The data used to create this figure are available.)

proportion for SPACA is ∼60.4 vol.%, which is beyond the high-Plg end of the mineralogical range for SPA impact melt differentiation products (Figure 4, 3.0–55.2 vol.% Plg). The observed composition and modal mineralogy of the SPACA would require either a more Al-enriched starting composition of SPA impact melt differentiation or additional contribution from post-SPA processes (e.g., feldspathic ejecta from post-SPA basins).

More Al-enriched initial compositions for SPA impact melt would indicate that more crustal materials went into the melt. During the transient crater collapse stage of large impact events, the crust would migrate back in toward the basin center (Freed et al. 2014). Hence, it is suggested that the crust was not entirely removed in the SPA-forming impact (Trowbridge et al. 2020). As shown by the elliptical structure of topographical and compositional distribution of the SPA surface expression (Garrick-Bethell & Zuber 2009), the SPA formation process was likely an oblique impact although the vertical case is preferred in most SPA impact simulations (e.g., Potter et al. 2012). Recent three-dimensional models have attempted to take the elliptical nature of the SPA impact into account (e.g., Melosh et al. 2017); an oblique SPA impact would have incorporated a greater proportion of feldspathic crustal materials into the melt (Vaughan & Head 2014). Contamination (∼50%) of crustal materials into the SPA impact melt has been examined, while the modeled differentiation results of a contaminated SPA impact melt reveal that the additional Al may not affect the top (∼5 km thick) noritic layer. Instead, these added crustal materials resulted in earlier saturation of plagioclase and a (∼3 km) thicker layer of deep-seated plagioclase-bearing lithologies (Hurwitz & Kring 2014). Unless the SPA impact melt did not differentiate and the crustal materials directly contributed to the compositions of

solidified surface, the observed Al-rich composition of the SPACA surface is more likely from post-SPA processes.

Considering that the SPA region experienced numerous impact events in the long history (>4.3 Ga) since its formation (Wilhelms et al. 1987), materials ejected from more feldspathic regions outside the basin floor may account for a considerable proportion of the SPACA. The nearest potential source is the so-called Mg-pyroxene annulus (MPA) (Moriarty 2016), where the pyroxene composition is more Mg rich (64.8 Mg#) compared to the SPACA (58.2 Mg#). The mineral map products from the Kaguya MI data sets (Lemelin et al. 2016) reveal that MPA is more feldspathic (66.1 vol.% Plg) than SPACA (60.4 vol.% Plg) and meets the requirement as a candidate. The irregular boundary of SPACA is obviously shaped by those adjacent basins and large craters in MPA (Figure A1). The ejecta of these large impacts is believed to have contaminated the SPACA with MPA materials. Besides MPA, another potential source of feldspathic materials is the highlands outside the SPA basin. Although the feldspathic upper crust may have been removed by the SPA impact, distal ejecta from post-SPA basins could feed feldspathic materials back into the SPA basin floor (e.g., Xiao et al. 2021). This issue (contribution from post-SPA bombardments) was also discussed in the work of Petro & Pieters (2004, 2006). They found that some portion (20%–50%) of material at the surface of the SPA basin floor is introduced from the exterior of SPA, while it would not be enough to mask the SPA impact melt products. Ultimately, only the large (e.g., Imbrium) or adjacent basins (e.g., Apollo, Ingenii) could move the appreciable amount of material into the interior of SPA. Our unmixing results also suggest that the proportion of materials from the feldspathic upper crust outside the SPA is lower than 4.5 vol.% (versus 41.4–65.7 vol.% materials from MPA).

The thickness distribution of post-SPA impact ejecta provides further evidence of SPACA being contaminated by more feldspathic materials. Based on the transient cavity size and impact ejecta thickness estimation models (Pike 1974), it yields a post-SPA ejecta thickness of up to ~1.5 km in the current range of SPACA (Figure A1).

Assuming that the initial SPACA surface is formed in the SPA impact melt sheet, the surface regolith observed today could be regarded as a mixture of initial SPA impact melt products and post-SPA ejecta. Given the predicted compositions of the initial top noritic layer of the differentiated SPA impact melt sheet (Hurwitz & Kring 2014), results from applying linear unmixing procedures to the observed mineralogy show that post-SPA ejecta accounts for 70.2 vol.% of the materials of SPACA. With a significant contribution from feldspathic (MPA and highlands) end-members, unmixing analysis of average soil mineralogy indicates that another end-member for mixing is Fe, ITE (incompatible trace elements)-enriched materials (16.9–18.9 wt.% FeO, 3.1–6.7 ppm Th). Accordingly, the compositions of the CE-4 landing site (C) and the SPACA (S) are not represented by any known lithologies in the Apollo and Luna collections (Figure A7).

5. Conclusion and Perspective

Based on the VNIS data obtained from the CE-4 mission, we investigated the mineralogical properties of regolith encountered by the Yutu-2 rover and their implications for SPACA. The major outcomes of this study are as follows. The average plagioclase abundance of SPACA is beyond the high-plagioclase end of the mineralogical range of SPA impact melt differentiation products and would require an additional contribution from crustal materials. We suggest that either the crust was not entirely removed in the SPA-forming impact or the ejecta from post-SPA basins fed feldspathic materials back onto the SPA basin floor. These analyses highlight the significance of plagioclase and crustal materials in mineralogical investigations and future explorations of the SPA basin (and the Moon).

Appendix

A.1. Hapke Radiative Transfer Model

The single scattering albedo single scattering albedo (SSA; ω) of mafic minerals in the VNIS spectral range (450–2395 nm) are modeled based on the refractive index ($n+ik$) and particle diameter (D) as follows (Hapke 2012):

$$\omega = S_e + (1 - S_e)(1 - S_i)\frac{\Theta}{1 - S_i\Theta} \tag{1}$$

$$S_e = \frac{(n-1)^2}{(n+1)^2} + 0.05 \tag{2}$$

$$S_i = 1 - \frac{4}{n(n+1)^2} \tag{3}$$

$$\Theta = e^{-\alpha\langle D \rangle} \tag{4}$$

$$\alpha = 4\pi k/\lambda \tag{5}$$

$$\langle D \rangle = \frac{2}{3}\left[n^2 - \frac{1}{n}(n^2 - 1)^{3/2}\right]D \tag{6}$$

The grain size (D) is held to a constant value of 17 μm as VNIR spectral properties of lunar soils are dominated by the 10–20 μm size fraction (Pieters et al. 1993).

The real part of the refractive index (n) for mafic minerals dependent on the mineral compositions (represented by Mg# (100 x molar Mg/(Mg+Fe))) is calculated using Equations (7)–(9):

$$n_{\text{LCP}} = 1.768 - 0.118 \times \text{Mg\#}/100 \tag{7}$$

$$n_{\text{HCP}} = 1.726 - 0.082 \times \text{Mg\#}/100 \tag{8}$$

$$n_{\text{Olv}} = 1.827 - 0.192 \times \text{Mg\#}/100 \tag{9}$$

The imaginary part of the refractive index (k) for mafic minerals as a function of mineral composition is calculated with the use of parameters derived from the least-squares regression of modified gaussian model (MGM) fitting results from Trang et al. (2013).

For Plg end-members, the optical constant n dependent on An# (molar Ca/(Ca+Na)) could be calculated based on Equation (12) from Warell & Davidsson (2010) as follows:

$$n_{\text{Plg}} = 1.523 + 0.0227 \times \text{An\#} + 0.0264 \times (\text{An\#})^2. \tag{10}$$

Given the narrow compositional range of lunar Plg, the n of Plg is set to a fixed value (1.57) in this study. The k of Plg was calculated from the RELAB (Reflectance Experiment LABoratory) reflectance spectrum with the n and D of the lunar plagioclase sample (LR-CMP-171 from the Apollo sample 15555,965 ($D < 125$ μm)) and the USGS (United States Geological Survey) spectral library of a terrestrial anorthite sample (HS201.3B, Sun & Lucey 2021).

The space-weathering effects of npFe and SMFe were quantified with the theories described in Lucey & Riner (2011):

$$\alpha_{sw} = \alpha_h + \alpha_c + \alpha_g = \frac{4\pi k_h}{\lambda} + \frac{36\pi z M_c \rho_h}{\lambda \rho_{\text{Fe}}} + \frac{3q_a M_g \rho_h}{D_{\text{Fe}} \rho_{\text{Fe}}} \tag{11}$$

$$z = \frac{n_{\text{Fe}} k_{\text{Fe}} n_h^3}{(n_{\text{Fe}}^2 - k_{\text{Fe}}^2 + 2n_h^2)^2 + (2n_{\text{Fe}} k_{\text{Fe}})^2} \tag{12}$$

where α_{sw} is the absorption coefficient of space-weathered minerals as a sum of absorption coefficients of host materials (α_h) and metallic Fe in the coatings (α_c) and grains (α_g). n_h and k_h are optical constants of host materials. λ is wavelength in units of micron. The optical constants of metallic Fe recently reported by Cahill et al. (2019) are linearly interpolated to the CE-4 VNIS bands. M_c and M_g are the mass fractions of metallic Fe in the grain and coating. ρ_h and ρ_{Fe} are the densities of host materials and metallic Fe. The density of metallic Fe and Plg is set to 7.6 and 2.75, respectively. The solid solution density of mafic minerals is calculated as the weighted average of the
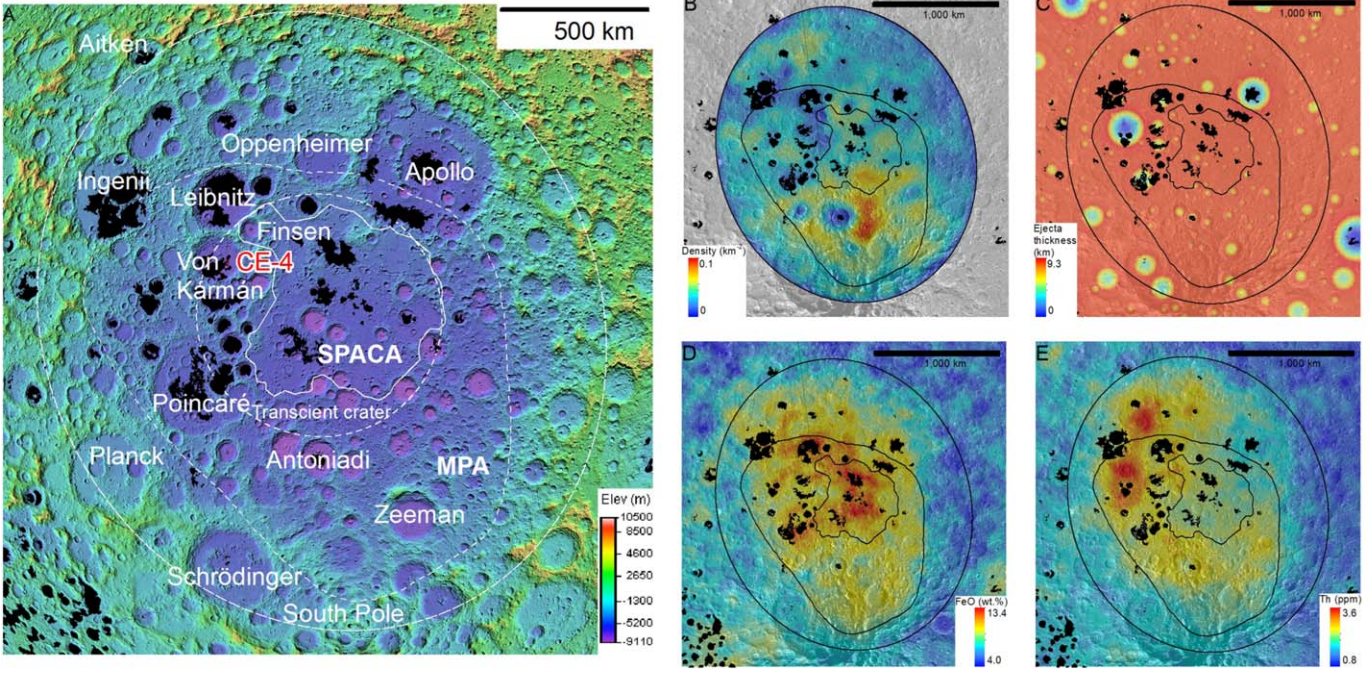
Figure A1. SPA region as seen in different data sets. (A) LOLA color shaded relief map (https://astrogeology.usgs.gov/search/map/Moon/LMMP/LOLA-derived/Lunar_LRO_LOLA_ClrShade_Global_128ppd_v04) centered on Mons Marguerite. The dashed circle is determined by the diameter (820 km) of the transient cavity formed by the SPA impact event from Hurwitz & Kring (2014), that is perfectly outlining the SPACA region identified by Moriarty (2016). The irregular dashed polygon is the extent of the so-called MPA. (B) Impact crater density calculated based on the lunar crater database from Robbins (2019). Note the high-density annulus of the secondary craters surrounding the Imbrian crater Antoniadi. (C) Ejecta thickness distribution of post-SPA impacts (>15 km). (D)–(E) LPGRS Half Degree Abundance Data of FeO and Th (https://pds-geosciences.wustl.edu/missions/lunarp/reduced_special.html). The boundary of SPACA identified by Moriarty (2016) is shown as an irregular polygon. The elliptical lines are the SPA basin ring. The black mask represents mare basalt regions modified from Nelson et al. (2014).

(The data used to create this figure are available.)

end-member density based on Webmineral data as follows:

$$\rho_{\text{Olv}} = 3.22 \times \text{Mg\#}/100 + 4.39 \times (100 - \text{Mg\#})/100, \tag{13}$$

$$\rho_{\text{LCP}} = 3.21 \times \text{Mg\#}/100 + 3.96 \times (100 - \text{Mg\#})/100, \tag{14}$$

$$\rho_{\text{HCP}} = 3.22 \times \text{Mg\#}/100 + 3.56 \times (100 - \text{Mg\#})/100. \tag{15}$$

q_a is the absorption efficiency of metallic Fe computed from Mie theory (Bohren & Huffman 2008). The particle diameter of metallic Fe (D_{Fe}) in grains is adjusted to 0.8 μm.

After the treatment of space-weathering effects, the total SSA of the mineral mixture was calculated as the weighted average of the end-member SSA of space-weathered minerals as follows (Hapke 2012):

$$\omega = \left(\sum_j \frac{M_j \omega_j}{\rho_j D_j}\right) \bigg/ \left(\sum_j \frac{M_j}{\rho_j D_j}\right), \tag{16}$$

where M_j, ω_j, ρ_j, and D_j are mass fraction, SSA, density, and grain size of the jth end-member.

The reflectance spectra of mineral mixtures could be predicted from the average SSA of mineral mixtures by forward modeling of the Hapke RTM.

The RTM used in this work is approximated as follows (Hapke 2012; Sun & Lucey 2021):

$$\text{REFF}(i, e, g) = K\frac{\omega}{4}\frac{1}{\mu_0 + \mu}\{p(g)[1 + B_S(g)] \\ + H(\mu_0/K)H(\mu/K) - 1\} \tag{17}$$

$$K = \frac{-\ln(1 - 1.209\phi^{2/3})}{1.209\phi^{2/3}}, \tag{18}$$

where $\phi = 0.41$ for lunar regolith (Sun & Lucey 2021),

$$\mu_0 = \cos(i) \tag{19}$$

$$\mu = \cos(e) \tag{20}$$

$$p(g) = 1 + b\cos(g) + c(1.5\cos^2(g) - 0.5). \tag{21}$$

The values of $b = -0.4$ and $c = 0.25$ were approximated for photometrically corrected spectra ($g = 30°$) (Sun & Lucey 2021),

$$B_S(g) = \left(1 + \frac{1}{h_S}\tan\frac{g}{2}\right)^{-1}, \tag{22}$$

$$h_S = \frac{3\sqrt{3}}{8}\frac{K\phi}{\ln(1000)}, \tag{23}$$

$$H(x) = \frac{1 + 2x}{1 + 2\gamma x}, \tag{24}$$

$$\gamma = \sqrt{1 - \omega}. \tag{25}$$

To verify the robustness of our spectral LUT, the RELAB spectra of 19 Apollo soil samples were matched with the spectral LUT to estimate the mineralogy and compare with

their modal mineralogy characterized by LSCC (Taylor et al. 2001). Two different criteria (RMSE and SA) were used to find the best match between the spectral LUT and LSCC spectra. The RMSE and SA are calculated as follows:

$$\mathrm{RMSE} = \sqrt{\frac{1}{m}\sum_{i=1}^{m}(y_{i,\mathrm{measured}} - y_{i,\mathrm{modeled}})^2}, \qquad (26)$$

$$\mathrm{SA} = \cos^{-1}\left(\frac{y_{\mathrm{measured}}^{T} y_{\mathrm{modeled}}}{\sqrt{y_{\mathrm{measured}}^{T} y_{\mathrm{measured}}} \sqrt{y_{\mathrm{modeled}}^{T} y_{\mathrm{modeled}}}}\right). \qquad (27)$$

The superscript "T" represents transposition. The spectral matching returned excellent results (Figure 2) that the RMSE and SA between the modeled and observed spectra are lower than 0.005. The mineral abundances of 18 soil samples (except 71061) modeled with our LUT exhibit a correlation of 0.96 and an RMSE of 6.53 vol.% versus their modal mineralogy quantified by LSCC. The RMSE/SA between the modeled and CE-4 VNIS spectra are lower than 0.03 for soil targets.

A.2. Estimation of Impact Ejecta Thickness

Ejecta thickness of post-SPA impacts were calculated using the model proposed by Pike (1974):

$$T_E = 0.033 R_t (r/R_t)^{-3.0} \qquad (28)$$

where T_E is the ejecta thickness at a distance r in units of meters, and R_t is the rim radius of the transient cavity in meters and could be inverted as follows (Kring 1995):

$$R_t = \sqrt[1.07]{R_C/0.86}, \qquad (29)$$

where R_C is the current radius of the crater/basin. r is the distance from the crater/basin center in meters and is defined as the spherical distance as follows:

$$D(x1, y1, x2, y2) = R_M * \cos^{-1}(\sin(x1)*\sin(x2) + \cos(x1)*\cos(x2)*\cos(y1 - y2)), \qquad (30)$$

where $(x1, y1)$ and $(x2, y2)$ are the longitudes and latitudes of two points, and R_M is the radius of the Moon (1737.4 km).

A.3. Effects of the SG Smoothing Algorithm on BC and IBDR

The CE-4 VNIS reflectance spectra present noisy (fluctuant) variations with wavelength (e.g., Figure A2). Therefore, the Savitzky-Golay (SG) smoothing algorithm (Savitzky & Golay 1964) was used to reduce the effects of local noises on the automatic detection of tie points for continuum removal with the tangency line method and on the calculation of the band center (BC) and IBD values (Table A1). The order of the SG smoothing algorithm is set to 5 because the VNIS spectrum has nominally four minimum/maximum points (i.e., the short-wavelength maximum of 1 μm absorption at ∼700–750 nm, minimum of 1 μm absorption, maximum between 1 μm and 2 μm absorptions at ∼1400–1700 nm, minimum of 2 μm absorption). We tested the resulting BC and IBD values with all possible numbers of points in the smoothing window (i.e., 7–389 points, Figure A8). As shown in Figure A8, when the number of points is between 8 and 40, the SG smoothing algorithm has negligible effects on the BC1 values (966.0 ± 0.6). Furthermore, the BC2 (2204.6 ± 2.3) and IBDR (0.97 ± 0.04) values exhibit relative uncertainties below 4%. Compared to the BC and IBDR values derived from the unsmoothed spectrum, the difference in BC1 values (∼1.0 nm) is negligible. However, the differences in the BC2 and IBDR values between unsmoothed and smoothed spectra are large (∼32.4 nm for BC2 and 0.36 for IBDR, respectively). In summary, we suggest that an SG smoothing algorithm with number of points between 8 and 40 and an order of 5 would
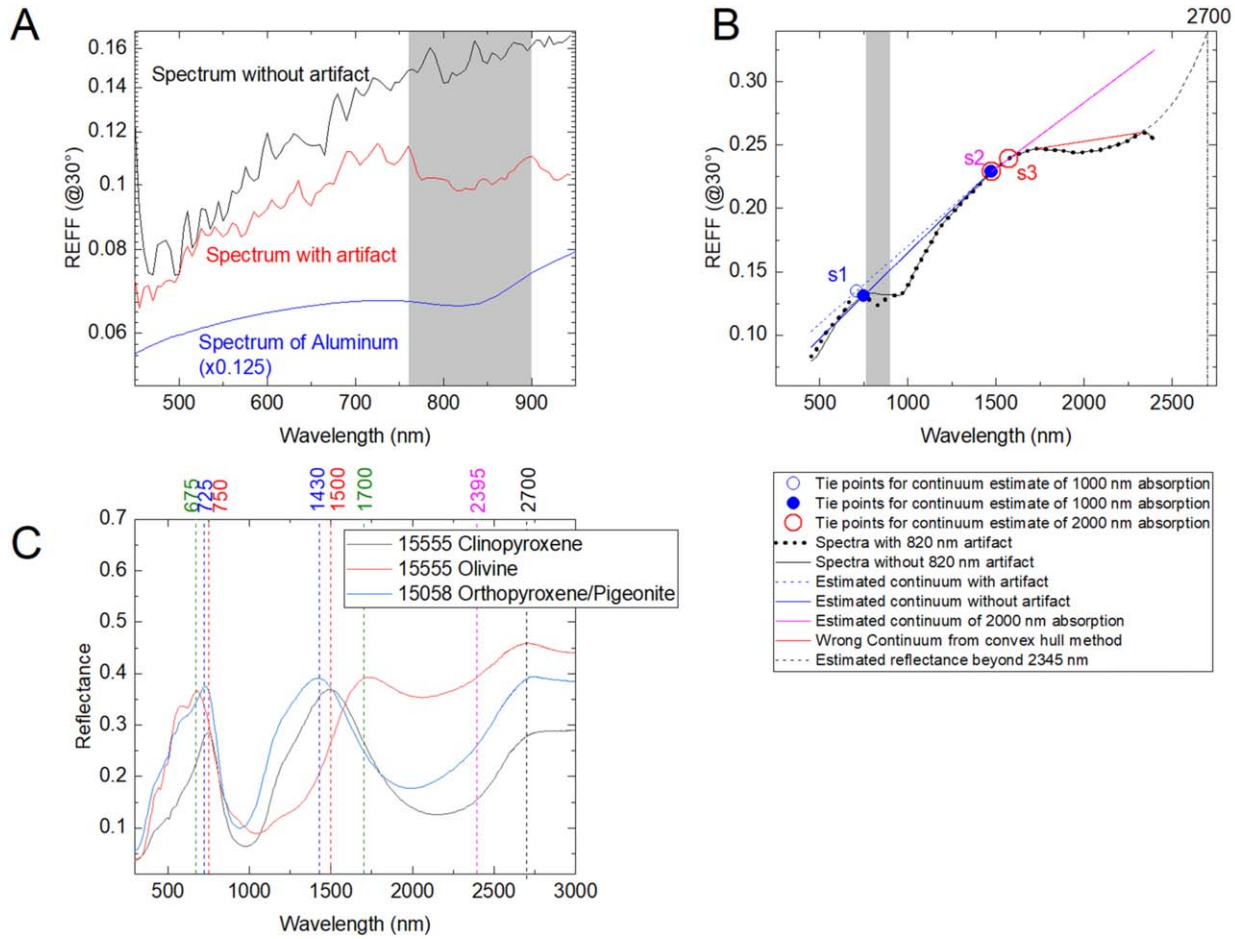
Figure A2. The 820 nm artifact in VNIS spectra and its effects on continuum removal. (A) The artifact (gray region) between 760 nm and 900 nm. (B) The artifact affects the positions of the tie point used for continuum removal of CE-4 VNIS data. (C) VNIR spectra of lunar clinopyroxene, olivine, and orthopyroxene/pigeonite collected and characterized by the Apollo missions (Data are from RELAB database: clinopyroxene (LR-CMP-168 from Apollo 15 sample 15555), olivine (LR-CMP-169 from Apollo 15 sample 15555), and orthopyroxene (LR-CMP-173 from Apollo 15 sample 15058). The endpoint wavelength (2395 nm) of VNIS spectra is marked by a magenta dashed line to illustrate that the 2 μm absorption band was not completely measured by VNIS.

(The data used to create this figure are available.)

A.4. Mixing Effects in CE-4 Soils

Because CE-4 landed in the VKB zone affected by FE, ballistic ejecta from the Finsen crater should mix to some degree with local Von Kármán materials during emplacement (Oberbeck 1975). Unmixing analyses were used to identify the FE component in CE-4 VNIS data (Figure A4). Given that the basaltic deposits in the Von Kármán crater floor have been mostly obscured by nonmare crater ejecta, the VKB end-member for mixing was defined by the basaltic ejecta of the Zhinyu crater, which presents the highest FeO contents (>15 wt.%, pure mare area, Gillis et al. 2003) in the floor of the Von Kármán crater. The modal mineralogy and FeO contents derived from orbital observations using data from the Kaguya multiband imager (MI) (Lemelin et al. 2016) reveal continuous compositional and mineralogical variations along the section line Zhinyu-CE4-Finsen (Figure A4). The Plg proportion increases from Zhinyu to the continuous ejecta that surrounds

improve the spectral quality of 1 μm absorption in VNIS data but bring in a relative difference below 4% for 2 μm absorption and a larger relative difference of 37% for IBDR values in comparison with those from unsmoothed spectra.

Table A1
Definitions of Spectral Indices Used in This Work

Spectral Index	Definition
BD940	$\frac{R(740\ \mathrm{nm})}{R(940\ \mathrm{nm})}$
IBD820	$\sum_{n=0}^{28}(1 - \frac{R(760 + 5 \times n)}{R_C(760 + 5 \times n)})$
IBD1000	$\sum_{n=0}^{(s2-s1)/5}(1 - \frac{R(s1 + 5 \times n)}{R_C(s1 + 5 \times n)})$
IBD2000	$2 \times \sum_{n=0}^{(BC2-s3)/5}(1 - \frac{R(s3 + 5 \times n)}{R_C(s3 + 5 \times n)})$
IBDR	$\frac{IBD2000}{IBD1000}$

Note. s1, s2, and s3 are the three points used to define the continuum (Figure A2), BC1 and BC2 are the band centers of the 1 μm and 2 μm absorptions, R is the spectral reflectance data at the given wavelength, and R_C is the continuum value at the given wavelength.

the Finsen crater rim (1–2 radius) while the mafic mineral abundances and FeO contents both decrease from Zhinyu to Finsen. The central peak of Finsen exhibits a different mineralogy (LCP-richer, Figure A4) from FW and FE, hence SPACA data sets (not associated with Finsen) were also included for comparison (Figure A6). The composition and
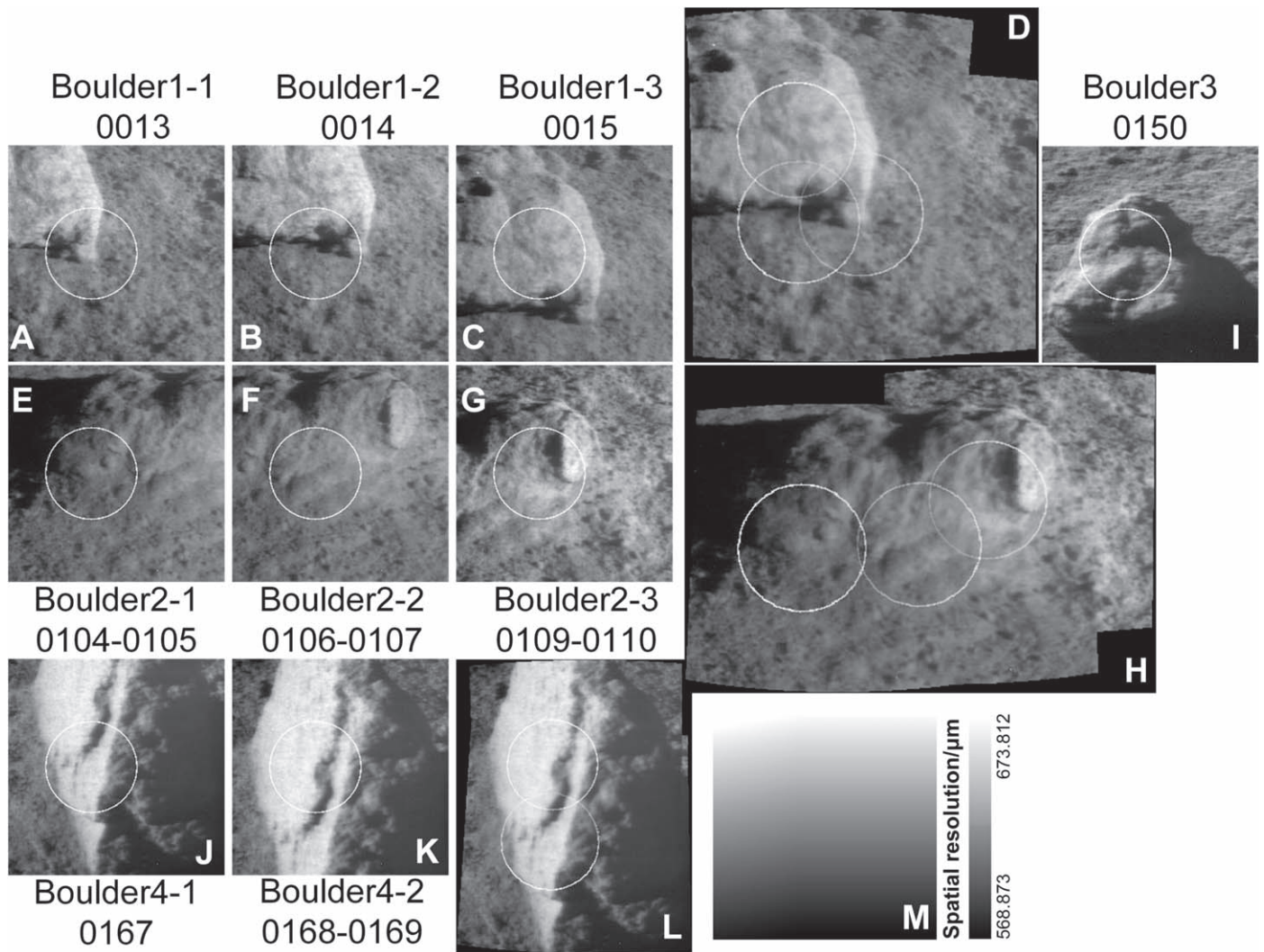
Figure A3. 900 nm band images of VNIS detections for boulders. (A)–(C) images of the boulder measured on the third lunar day. (D) Mosaic of A–C. (E–G) images of the boulder measured on the 13th lunar day. (H) Mosaic of E–G. (I) image of the boulder measured on the 23rd lunar day. (J)–(K) Images of the boulder measured on the 26th lunar day. (L) mosaic of J–K. (M) spatial resolutions of each pixel in the images. The white circles show the FOV (with a diameter of ∼65 mm projected onto the lunar surface) of the SWIR detectors. The VNIS spectra of different parts of boulders are shown in Figures 3B and 3D.

(The data used to create this figure are available.)

(The complete figure set (120 images) is available.)

mineralogy of SPACA (not associated with Finsen) resemble those exposed on the Finsen crater wall and continuous ejecta surrounding the crater rim.

Although the soils of the CE-4 landing region seen by both orbital and ground spectrometers are mixtures, an advantage of the CE-4 mission is that the VNIS aboard the Yutu-2 rover can make measurements on centimeter-sized boulders, which are not resolvable for orbital spectrometers. Individual boulders encountered by the Yutu-2 rover would commonly be Von Kármán basalts excavated by younger local craters (e.g., Zhinyu), but the first boulder with LCP-rich mafic mineralogy might be surviving blocks ejected from Finsen and represent an end-member for the mixing in local soils.

The modal mineralogy of boulders could be semiquantitatively determined based on the pixel classification assuming that the area fraction of pixels containing diagnostic 1 μm mafic absorption is equal to the volume percentage of mafic phases within the boulders. The pixels without obvious 1 μm absorptions could be regarded as a pure Plg pixel. This method is only valid for coarse-grained rocks with grain size larger than the pixel resolution (∼600 μm; Figure A3) and may not be suitable for estimating Plg and mafic mineral abundances in fine-grained rocks. For fine-grained rocks, most pixels are Plg intergrown with mafic minerals so that they exhibit mafic absorptions and the proportion of Plg will be underestimated based on the pixel classification. The fraction of pixels without mafic absorptions in VNIR images can be used as a lower estimate for Plg proportion in boulders.

The VNIR images could be also used to analyze the texture of boulders. As shown in Figure A9, the pixels with a strong 1 μm mafic absorption feature are probably mafic phenocrysts or clasts. The largest mafic grain/clast in the first boulder is about 65 pixels (∼3.9 cm) in the longest dimension. The texture (i.e., large mafic clast/phenocrysts in a fine-grained matrix) of the boulder would exclude the possibility of a plutonic origin. These results indicate the following lithologies:
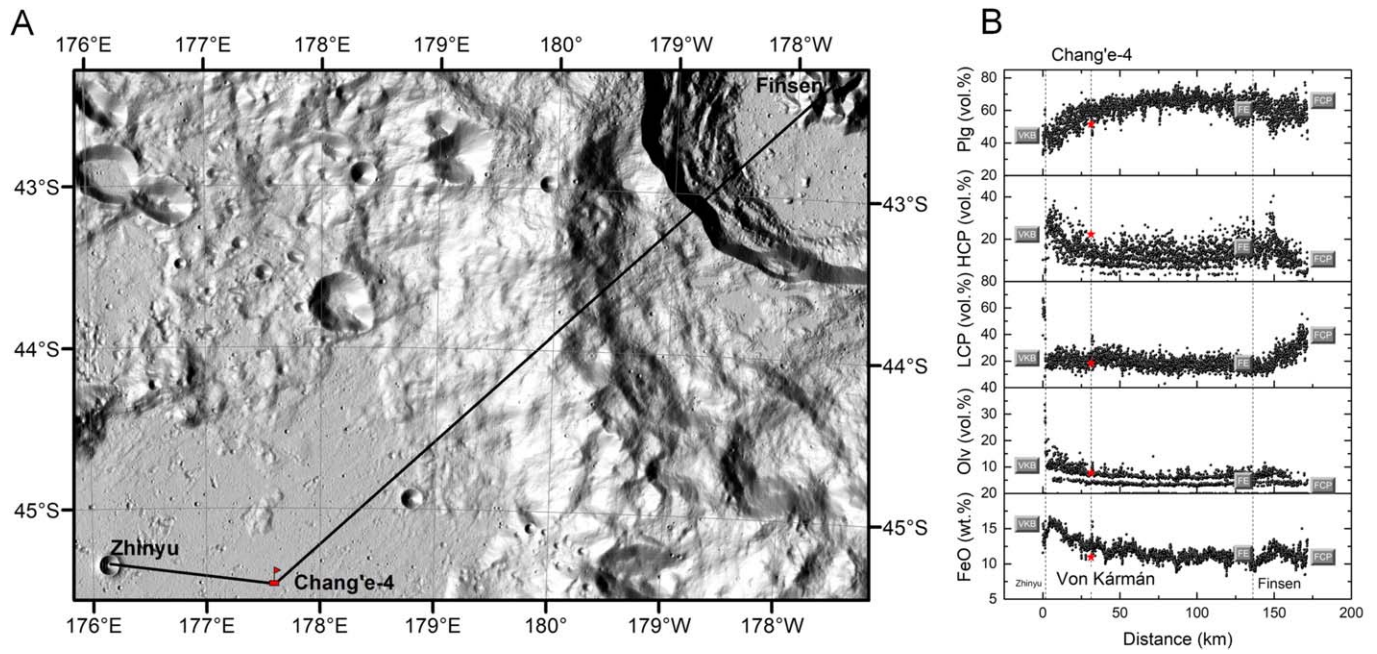
Figure A4. Compositional and mineralogical profile along the section line Zhinyu-CE4-Finsen. (A) Section line overlain on the shaded relief derived from LRO + Kaguya merged topography products (https://astrogeology.usgs.gov/search/map/Moon/LRO/LOLA/Lunar_LRO_LOLAKaguya_Shade_60N60S_512ppd). (B) Compositional and mineralogical variations along the traverse path. FeO and mineralogy data are from Kaguya MI global map products. Three dashed lines indicate the locations of the Zhinyu crater rim, CE-4 landing site, and Finsen crater rim on the section line. The red stars mark the mineralogy derived from CE-4 VNIS data sets. The dark marbles represent the three end-members for mixing, i.e., VKB, FE, and FCP (Finsen central peak).

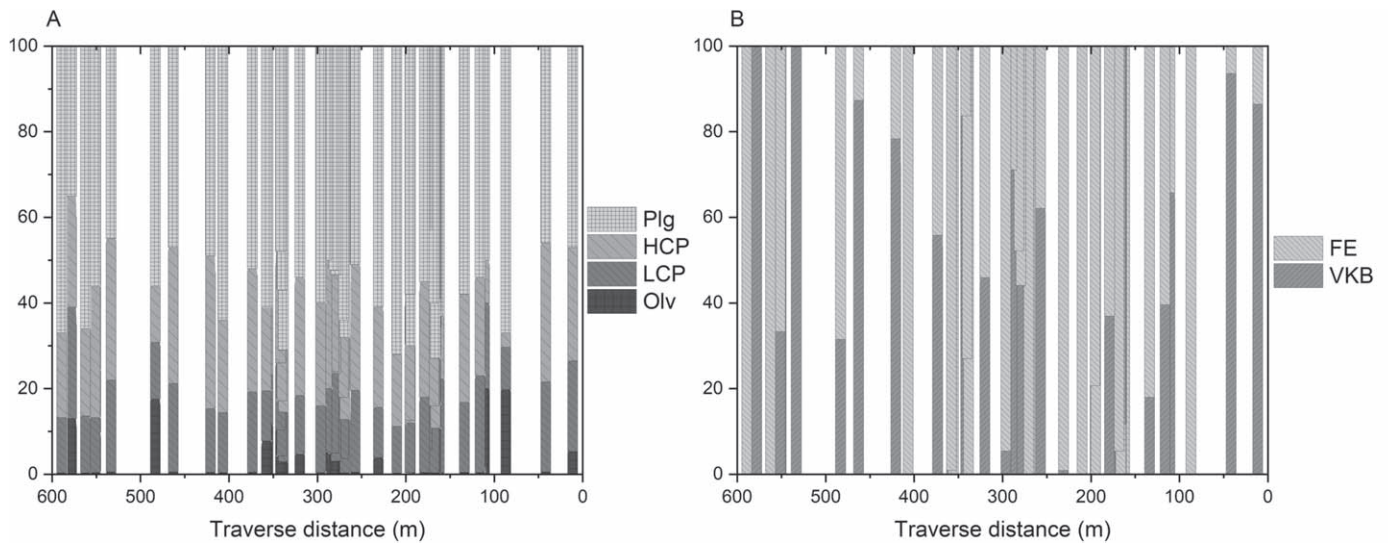(The data used to create this figure are available.)

Figure A5. Modal analyses of CE-4 soils. (A) Mineralogy. (B) Mixing ratio.

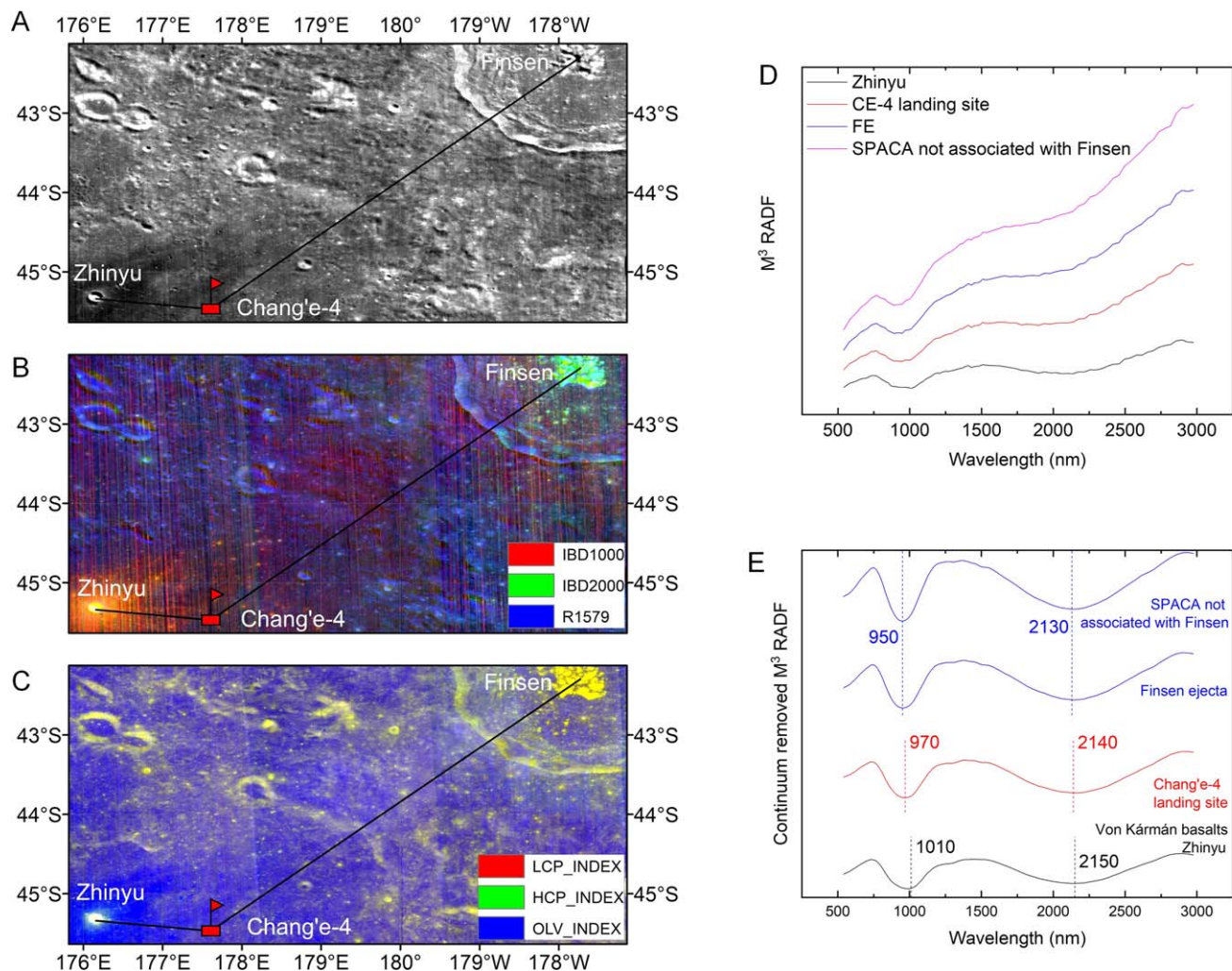(The data used to create this figure are available.)

Figure A6. Spectral and mineralogical profile along the section line Zhinyu-CE4-Finsen. (A). Mosaic of the Zhinyu-CE4-Finsen region at 540 nm from the M³ data sets (https://pdsimage2.wr.usgs.gov/archive/chandrayaan_1/m3/). (B) M³ Standard color composite. (C) Composite of mineral indices. IBD parameters and mineral indices are defined in Table A1 and Chen et al. (2020). (D) M³ RADF reflectance spectra of the Von Kármán basalts (VKB exposed by Zhinyu), CE-4 landing site, Finsen ejecta (FE), and SPACA region (not associated with Finsen). (E) Continuum-removed spectra.

(The data used to create this figure are available.)

(1) shock-lithified regolith breccia; (2) recrystallized impact melt breccia; and (3) mafic-phyric basalt. The mafic-rich patches are likely remnants of pristine mafic lithologies in regolith/melt breccia. Alternatively, the mafic patches also could be phenocrysts in a basalt.

The first boulder is a mafic clast-bearing melt/regolith breccia probably originating from a pristine lithology of norite/gabbro or mafic-phyric basalt. Although the pyroxene is dominated by LCP, whether it is orthopyroxene or pigeonite is unknown because they share similar spectral absorption features. A feldspathic mineralogy (60–80 vol.% Plg obtained from comparison with the RELAB spectral library of returned lunar rocks and meteorites) and source region (Zhinyu crater) were reported for the first boulder (Ma et al. 2020). As a distal ejecta from Zhinyu, the boulder is expected to have been launched from the target surface of the Zhinyu impact, which is either mare basalt or Finsen ejecta according to the stratigraphic studies (e.g., Qiao et al. 2019). The Plg-rich mineralogy of the boulder reported by Ma et al. (2020) is obviously not basaltic, but the other scenario of relaunching Finsen ejecta from the

Zhinyu crater to the CE-4 landing region is possibly responsible for adding mafic clasts into the fine-grained matrix.

A.5. Mantle Materials Identified by CE-4?

Although basin-forming events could breach the lunar crust and may have exposed mantle materials (e.g., Yamamoto et al. 2010), few mantle samples have been identified in the Apollo and Luna samples and in lunar meteorites up to now. Apollo 17 sample 74275 may contain mantle clasts (Shearer et al. 2015) but their mantle origin did not arrive at a consensus. The excavated mantle materials have been contaminated by crustal signatures and diluted in postbasin processes.

The soils of the CE-4 landing site were interpreted by some early researchers as originating from the lunar mantle (Li et al. 2019); however, their conclusion is based only on the presence of low-Ca pyroxene and olivine and lacks the key constraint from plagioclase abundance. Moreover, even if the soils measured by CE-4 VNIS were ultramafic, they cannot be interpreted as mantle materials. Typical counterexamples are the dunite samples collected from the Apollo 14 and 17 landing
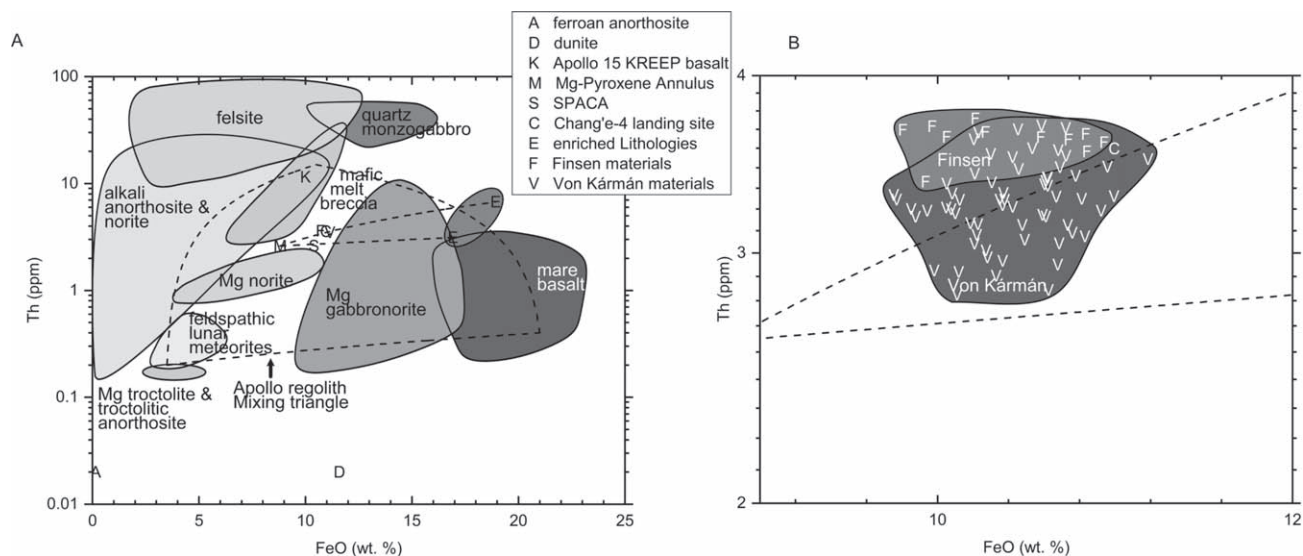
Figure A7. FeO-Th diagrams of lunar materials. (A) FeO-Th compositions of lunar rock samples modified from Jolliff et al. (2006). The fields with different grayscales represent compositional ranges of different lithologies that occurred in Apollo and Luna rock samples. The "A" point represents the highly feldspathic ferroan anorthosite sample 15418. The "C" point represents the regolith composition of the CE-4 landing site and the traverse area as seen by the Lunar Prospector gamma-ray spectrometer. The "D" point represents the Apollo 17 dunite sample 72415–7. The "E" points represent the enriched end-member lithologies for the mixing in SPACA. The "K" point represents the average compositions of Apollo 15 KREEP basalt samples. The "S" point represents the average compositions of SPACA. The dotted curves indicate mixing effects in lunar regolith samples among three end-members (i.e., feldspathic highlands materials, mare basalt, and KREEP-bearing materials). (B) Data used to unmix the Finsen materials ("F" points) and Von Kármán materials ("V" points).

(The data used to create this figure are available.)
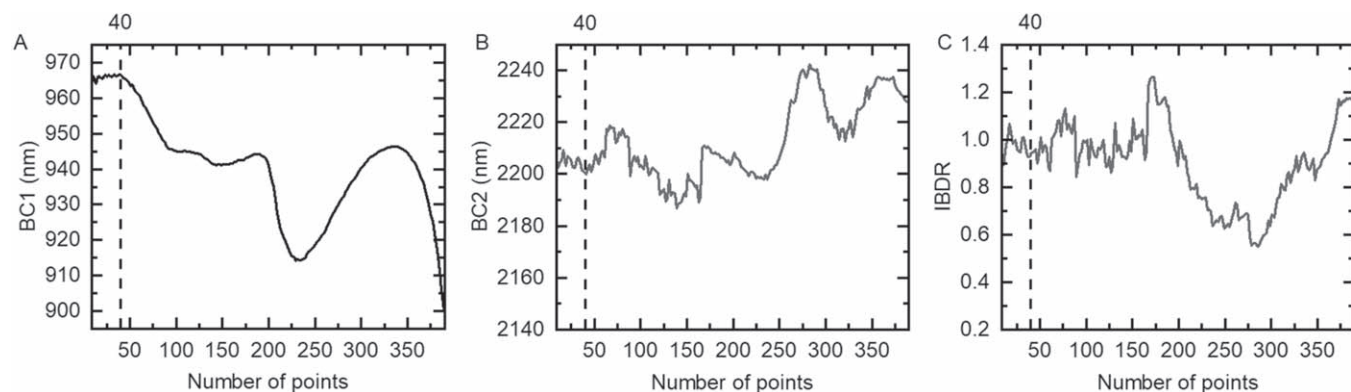

Figure A8. Variations of BC1, BC2, and IBDR values with different SG smoothing windows.

(The data used to create this figure are available.)

sites. Those dunite samples consist of 90–95 vol.% Mg-rich Olv (Fo$_{86-90}$) yet they are interpreted as resulting from the accumulation of olivine crystallized in crustal environments owing to their ITE-enriched parental melts and petrogenetic relationships to Mg-suite and mare basalt magmatism (e.g., Shearer & Papike 2005). Unfortunately, the trace element and isotopic information cannot be retrieved by the VNIR spectroscopy employed by the CE-4 mission. The mineralogy of regolith at the CE-4 landing region cannot directly represent the mafic assemblages in the lunar mantle. The melting, mixing with crustal materials, and fractional crystallization have altered the petrogenetic information inherited from mantle reservoirs even if these materials were initially sourced from the lunar mantle.

The end-member lithologies with Fe and ITE enrichments (mafic clasts in the first boulder) are consistent with a possible origin from differentiated SPA impact melt. The subsequently erupted basalts also could be mixed with the enriched materials by lava flow assimilation and continuous impact gardening. These enriched materials were diluted by more feldspathic ejecta, and a less mafic upper regolith layer was developed in SPACA and observed by orbital spectrometers. Some of these mixing products were delivered by the Finsen impact event and observed by the CE-4 VNIS. The enriched end-member lithologies are recorded as mafic clasts in a feldspathic matrix (as shown in the first boulder). To further reveal the nature of these mafic lithologies, future orbital spacecraft with high-enough spatial resolution to resolve these ancient fragments or landed missions with more advanced in-situ analytical techniques are required. Undoubtedly, returning samples from the SPACA would significantly contribute to a better understanding of the impact melt evolution and mare volcanism in this enormous basin and of the underlying lunar mantle.
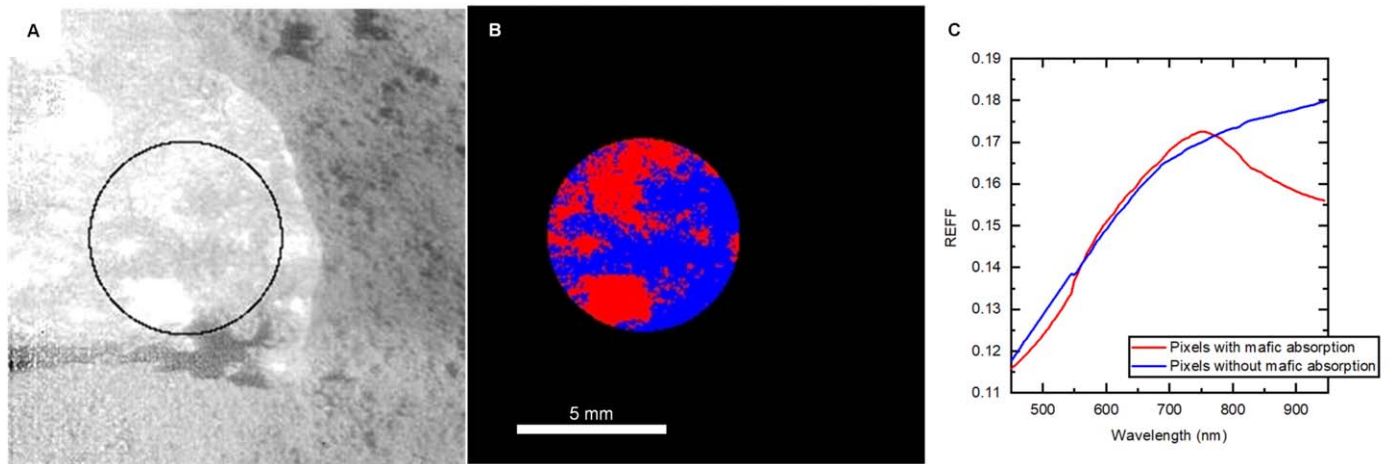
14

Figure A9. Spectral classification of VNIS images of the first boulder (0015). The circles indicate the FOV of the SWIR detector. (A) BD940 image. (B) Binary classification results with a pixel resolution of ∼600 μm. (C) Mean spectra (normalized at 750 nm) of blue pixels (with mafic absorptions) and red pixels (without mafic absorptions).

(The data used to create this figure are available.)

ORCID iDs

Le Qiao ⓘ https://orcid.org/0000-0002-6180-2344
Jiang Zhang ⓘ https://orcid.org/0000-0002-8369-871X

References

Bohren, C. F., & Huffman, D. R. 2008, Absorption and scattering of light by small particles (New York: Wiley)
Cahill, J. T., Blewett, D. T., Nguyen, N. V., et al. 2019, Icar, 317, 229
Chen, J., Ling, Z., Qiao, L., et al. 2020, Sci. China-Inf. Sci, 63, 140903
Di, K., Liu, Z., Liu, B., et al. 2019, JRemS, 23, 177
Freed, A. M., Johnson, B. C., Blair, D. M., et al. 2014, JGRE, 119, 2378
Garrick-Bethell, I., & Zuber, M. T. 2009, Icar, 204, 399
Gillis, J. J., Jolliff, B. L., & Elphic, R. C. 2003, JGRE, 108, 5009
Gou, S., Di, K., Yue, Z., et al. 2019, E&PSL, 528, 115829
Hapke, B. 2008, Icar, 195, 918
Hapke, B. 2012, Theory of Reflectance and Emittance Spectroscopy (Cambridge: Cambridge Univ. Press)
Hu, X., Ma, P., Yang, Y., et al. 2019, GeoRL, 46, 9439
Huang, J., Xiao, Z., Xiao, L., et al. 2020, Geo, 48, 723
Hurwitz, D. M., & Kring, D. A. 2014, JGRE, 119, 1110
Jia, Y., Zou, Y., Ping, J., et al. 2018, P&SS, 162, 207
Jolliff, B. L., Wieczorek, M. A., Shearer, C. K., et al. 2006, RvMG, 60, 1
Kring, D. A. 1995, JGRE, 100, 16979
Lemelin, M., Lucey, P. G., Gaddis, L. R., et al. 2016, LPSC, 47, 2994
Li, C., Liu, D., Liu, B., et al. 2019, Natur, 569, 378
Lin, H., He, Z., Yang, W., et al. 2020, NatSR, 7, 913
Liu, B., Li, C. L., Zhang, G. L., et al. 2014, RAA, 14, 1578
Lucey, P. G., & Riner, M. A. 2011, Icar, 212, 451
Ma, P., Sun, Y., Zhu, M. H., et al. 2020, Icar, 350, 113901
Melosh, H. J., Kendall, J., Horgan, B., et al. 2017, Geo, 45, 1063

Moriarty, D. P. 2016, PhD Thesis, Brown University
Morris, R. V. 1980, LPSC, 11, 1697
Nakamura, R., Matsunaga, T., Ogawa, Y., et al. 2009, GeoRL, 36, L22202
Nelson, D. M., Koeber, S. D., Daud, K., et al. 2014, LPSC, 45, 2861
Oberbeck, V. R. 1975, RvGeo, 13, 337
Petro, N. E., & Pieters, C. M. 2004, JGRE, 109, E06004
Petro, N. E., & Pieters, C. M. 2006, JGRE, 111, E09005
Pieters, C. M., Fischer, E. M., Rode, O., & Basu, A. 1993, JGR, 98, 20817
Pieters, C. M., Taylor, L. A., Noble, S. K., et al. 2000, M&PS, 35, 1101
Pieters, C. M., Tompkins, S., Head, J. W., et al. 1997, GeoRL, 24, 1903
Pike, R. J. 1974, E&PSL, 23, 265
Potter, R. W., Collins, G. S., Kiefer, W. S., et al. 2012, Icar, 220, 730
Qi, X., Ling, Z., Zhang, J., et al. 2020, RemS, 12, 3211
Qiao, L., Ling, Z., Fu, X., et al. 2019, Icar, 333, 37
Robbins, S. J. 2019, JGRE, 124, 871
Savitzky, A., & Golay, M. J. 1964, AnaCh, 36, 1627
Shearer, C. K., Burger, P. V., Bell, A. S., et al. 2015, M&PS, 50, 1449
Shearer, C. K., & Papike, J. J. 2005, GeCoA, 69, 3445
Spudis, P. D., Gillis, J. J., & Reisse, R. A. 1994, Sci, 266, 1848
Sun, L., & Lucey, P. G. 2021, JGRE, 126, e06691
Taylor, L. A., Pieters, C. M., Keller, L. P., et al. 2001, JGRE, 106, 27,985
Tompkins, S., & Pieters, C. M. 2010, M&PS, 45, 1152
Trang, D., Lucey, P. G., Gillis-Davis, J. J., et al. 2013, JGRE, 118, 708
Trowbridge, A. J., Johnson, B. C., Freed, A. M., et al. 2020, Icar, 352, 113995
Vaughan, W. M., & Head, J. W. 2014, P&SS, 91, 101
Warell, J., & Davidsson, B. J. R. 2010, Icar, 209, 164
Wilhelms, D. E., John, F., & Trask, N. J. 1987, The Geologic History of the Moon, US Geological Survey Professional Paper, 1348
Xiao, Z., Ding, C., Xie, M., et al. 2021, GeoRL, 48, e90935
Xu, J., Wang, M., Wang, R., et al. 2021, RemS, 13, 2359
Yamamoto, S., Nakamura, R., Matsunaga, T., et al. 2010, NatGe, 3, 533